

# Cosmic filaments confirm unexplained cooling of CMB photons in two independent redshift ranges

Juan Ignacio Domínguez Feldman<sup>\*</sup>

*Facultad de Matemática, Astronomía, Física y Computación (FAMAF), UNC, Córdoba, Argentina*

Luis A. Pereyra<sup>†</sup>

*Observatorio Astronómico de Córdoba (OAC), UNC, Córdoba, Argentina*

Frode K. Hansen<sup>‡</sup>

*Institute of Theoretical Astrophysics, University of Oslo, PO Box 1029 Blindern, 0315 Oslo, Norway*

Facundo Toscano<sup>§</sup>

*Instituto de Astronomía Teórica y Experimental (IATE), CONICET-UNC, Córdoba, Argentina*

Diego Garcia Lambas<sup>¶</sup>

*Instituto de Astronomía Teórica y Experimental (IATE), CONICET-UNC, Córdoba, Argentina  
Observatorio Astronómico de Córdoba (OAC), UNC, Córdoba, Argentina*

(Dated: June 11, 2025)

Recent papers have reported an unexplained cooling of CMB photons passing through galaxies in nearby cosmic filaments  $z < 0.02$  at the  $> 5\sigma$  level. Here we show for the first time that this effect is also present at higher redshifts  $0.02 < z < 0.04$ . Instead of calculating the CMB temperature around individual galaxies as in previous works, we analyze mean CMB temperature profiles associated to cosmic filaments in three dimensions. We have considered different thresholds in the linear K-band luminosity density of the filaments as a proxy to mass density. Furthermore, we have analyzed the dependence of the results on the average orientation of filaments with respect to the line of sight. These studies were implemented to test the expected dependence on mass density as well as on photon trajectory length within the cosmic filaments. We find a  $3 - 4\sigma$  detection of a temperature decrement trend towards the spine of the filaments, the larger the mass and the more radially oriented the filament, the stronger the temperature decrement. This trend is seen independently in both redshift ranges  $0.004 < z < 0.02$  and  $0.02 < z < 0.04$ . We therefore conclude that our results provide strong evidence for a lower CMB temperature along massive cosmic filaments in the nearby universe  $z < 0.04$ .

**Keywords:** Cosmology, Large-Scale Structure, Cosmic Microwave Background.

## I. INTRODUCTION

The prediction and subsequent discovery of the Cosmic Microwave Background (CMB) stands as one of the greatest breakthroughs of modern cosmology. Since then, detailed studies of the CMB have played a key role in the development of theoretical models of the universe. This remnant radiation from the early universe is remarkably homogeneous<sup>[1]</sup>, exhibiting only small-amplitude fluctuations<sup>[2]</sup>, which are fundamental for understanding the formation of present-day large-scale structures.

Among these structures are cosmic filaments, corresponding to elongated overdense regions tracing the highly anisotropic distribution of galaxies. These

filaments can extend over scales larger than 100 Mpc in length<sup>[3]</sup>, while their typical width along the spine is only a few Mpc<sup>[4]</sup>. In large-scale numerical simulations, filaments grow by gravitational instability from sparse coherent inhomogeneities in the expanding substratum<sup>[5, 6]</sup>. Within this framework, the present-day filaments of galaxies can be interpreted as direct evidence of significant gravitational compression perpendicular to the filament spine<sup>[7, 8]</sup>.

From the perspective of the matter content of the universe, filaments constitute a substantial fraction of both baryonic and dark matter in the  $\Lambda$ CDM model. Recent analyses of numerical simulations<sup>[5, 9]</sup> have further revealed distinct behaviors between short and long filaments: short filaments tend to collapse along their spine, while long filaments exhibit high expansion velocities along their spine axis.

Tanimura et al. 2020<sup>[10]</sup> investigated the hot gas associated with filaments identified in the Sloan Digital Sky Survey (SDSS)<sup>[11]</sup>, within the redshift range  $0.2 < z < 0.6$ . They detected thermal Sunyaev-

<sup>\*</sup> [juan.dominguez99@mi.unc.edu.ar](mailto:juan.dominguez99@mi.unc.edu.ar)

<sup>†</sup> [luis.pereyra@unc.edu.ar](mailto:luis.pereyra@unc.edu.ar)

<sup>‡</sup> [f.k.hansen@astro.uio.no](mailto:f.k.hansen@astro.uio.no)

<sup>§</sup> [facundo.toscano@mi.unc.edu.ar](mailto:facundo.toscano@mi.unc.edu.ar)

<sup>¶</sup> [diego.garcia.lambas@unc.edu.ar](mailto:diego.garcia.lambas@unc.edu.ar)

Zel'dovich (tSZ) signal in these structures with a significance of  $4.4\sigma$ , estimating the gas temperature to be around  $10^6 K$ . However, the tSZ effect in filaments is typically expected to be on the order of  $\sim 2\mu K$ .

Previous analysis by our group (Luparello et al. 2023 (L2023), Hansen et al. 2023 and 2025 (H2023 and H2025), Garcia Lambas et al. 2024 [12–15]) have shown that the observed CMB temperature around large, nearby spiral galaxies within  $z < 0.02$  is significantly lower than expected, as confirmed comparing to 10,000 Planck-like synthetic CMB simulations. The significance of this effect exceeds  $4\sigma$ . As noted in those works, the observed temperature decrement extends well beyond the virial radius of the galaxies, suggesting that large-scale inhomogeneities play an important role in this newly identified extragalactic systematic. In H2025, it was further shown that this effect becomes even more prominent in regions associated with the densest filaments—approximately half of the large spirals in the sample lie in such environments. When the largest angular scale modes of the CMB are removed from the analysis, reducing noise from intrinsic CMB fluctuations, the significance of the temperature profile goes to nearly  $6\sigma$ . The effect has also been confirmed by cross-correlating the nearby dark matter distribution with the CMB temperature field in [16].

Despite this, Toscano et al. 2025 [17] showed that masking regions around these galaxies does not significantly affect the estimation of cosmological parameters within the  $\Lambda$ CDM framework. Additionally, Hansen et al (2025b, in prep. H2025b) found that CMB photons passing through local voids ( $z < 0.03$ ) appear hotter than expected, with a significance of  $2.7 - 3.6\sigma$ , potentially pointing to a sign change of the Integrated Sachs-Wolfe (ISW) effect in the local universe.

Taking these findings into account, in this work we investigate the connection between the previously reported temperature decrement around overdense regions and the presence of filaments in the nearby universe. In particular, we will extend the redshift range beyond  $z < 0.02$  where the effect has been analysed and detected so far. We focus particularly on the densest filaments and those oriented along the line of sight, where the signal is expected to be strongest due to the longer trajectory length of the photons in these filaments. We will first attempt to confirm previous findings at the lowest redshifts  $z < 0.02$  using our new approach based on temperature profiles around filaments instead of independent galaxies, and then check if a similar signal may be present in the next redshift shell  $0.02 < z < 0.04$ .

The paper is organized as follows: In Section II we present the data used in this work, including the filament identification procedure and the CMB maps. Section III describes our methodology, including the compu-

tation of perpendicular distances to filament spines, the removal of large-scale multipoles and the calculation of CMB temperature profiles associated with the filaments. In Section IV, we present our main results, focusing on the dependence of the temperature profiles on filament luminosity density and orientation relative to the line of sight. Finally, Section V discusses the implications of our findings and summarizes the main conclusions.

## II. DATA

### A. Filament identification

In order to identify filaments, we have used the 2MASS Redshift Survey (2MRS) [18] galaxies as tracers [19]. This catalog contains 43533 galaxies complete in the K-band up to  $K_s = 11.75$ . The wide sky coverage of the 2MRS (91% of the sky) makes it ideal to identify nearby filaments of large angular extent and perform joint studies of the CMB and large-scale structures.

We have used galaxies with diameters larger than the median of the distribution ( $D > 8.5$  Kpc) as tracers, roughly corresponding to galaxies brighter than the  $M^*$  parameter of the Schechter luminosity function. We have worked on the redshift range  $0.004 < z < 0.040$ . The lower limit ( $\sim 1200 km s^{-1}$ ) is adopted in order to exclude galaxies in the very nearby universe where peculiar velocities are relatively large and redshifts do not provide a reliable measure of distance, strongly biasing the identification of filaments. The upper limit corresponds to the threshold where the tracer galaxies drop significantly, also affecting a reliable identification of filaments.

We have applied the DisPerSE [20, 21] code to this sample of galaxies in order to obtain our set of filaments. It is important to clarify that the filaments are defined as the joint of the straight lines that are traced between two nodes of the filament provided by the algorithm. We also notice that the redshift distribution of 2MRS tracers flattens beyond  $z = 0.020$  and we will adopt this intermediate threshold to consider two complementary subsamples ( $0.004 < z < 0.020$  and  $0.020 < z < 0.040$ ). Figure 1 shows the projected distribution of filaments for both redshift ranges. We notice that we cannot extend to further redshifts beyond  $z = 0.040$  since, as mentioned before, the galaxy tracers of the 2MRS catalog strongly decline, not allowing a reliable identification of filaments. The persistence parameter given to DisPerSE is  $\sigma = 4$ ; for this value, the fraction of false filaments detected is  $\sim 0.006\%$  [20]. The adopted cosmology in this work is  $\Omega_\Lambda = 0.6911$ ,  $\Omega_M = 0.3089$ ,  $\Omega_k = 0$  and  $H_0 = 67.74 Km s^{-1} Mpc^{-1}$ , consistent with Planck 2018 results [22].

## B. Filament properties

In order to characterize filaments properly, we have considered two properties: mean linear mass density and the angle between the filament and the line of sight.

The former is the ratio between the filament total mass and its length. We estimate a proxy of the filament total mass by the expected linear relation with the K-band luminosity associated to galaxies within the filaments. For this aim, we sum the K-band luminosity of galaxies within a perpendicular distance of  $d_{\perp} < 4$  Mpc from the filament spine. The length is defined as the sum of the individual lengths of each filament segment.

The latter is the angle between the extremal points of the filament and the radial direction. It is a measure of the global orientation of the filament with respect to the plane of the sky. This angle may be an important parameter for the effect produced by a given filament since we argue that the interaction between CMB photons and structures accumulates along of the line of sight. Similarly, we also expect a more significant signal for more dense filaments, so that the largest contribution to the CMB photons would be associated to the densest and most radially oriented filaments.

## C. CMB maps

We use CMB intensity maps taken by the Planck satellite from the Public Release 3 (PR3) [23] [24]. The Planck data were cleaned by 4 different foreground methods as described in Planck Collaboration, IV 2018 [25]. In general, the temperature maps for all 4 foreground methods agree very well, and in H2025 we made a thorough study of the differences on the CMB cooling in galactic halos, showing only small differences. For this reason, we will here focus on SMICA for PR3, but use SEVEM frequency cleaned maps for testing a possible frequency dependence of the signal. We use the Planck common mask created for PR3 [25] to mask possible galactic residuals, leaving 78% of the sky available for analysis. To process these maps we used Healpy [26] [27] with a `Nside` parameter value of 1024. The pixel area for this parameter is  $\Omega_p = 11.8026 \text{ arcmin}^2$ .

We will also use publicly available simulated Planck CMB maps which include known Planck systematic effects and noise properties which have been passed through the SMICA foreground cleaning pipeline. These simulations will be used to quantify the significance of our results. For a given CMB temperature bin, we will define significance as the distance from zero temperature given in units of standard deviations calculated from simulations. For most cases, we use 100 simulations to estimate the standard deviations, but for some test cases we also used 1000 simulations and found excellent agreement.

## III. METHODOLOGY

### A. Calculating transversal distances to filaments

Filaments projected on the two-dimensional sphere may produce complex structures as shown in Figure 1. In order to calculate distances perpendicular to the filamental spines, we developed a method independent of the sky projection structure. To accomplish this, for each projected segment of a filament, we search for all pixels within a rectangle of fixed projected area. Each rectangle spans 6 Mpc in the direction perpendicular to the filament axis. In order to convert this width to an angular width on the sky, we scale it according to the mean redshift of the segment, as we are interested in selecting pixels up to a fixed projected distance. Subsequently, we rotate the segment and all associated pixels so that the segment lies in the equatorial (x-y) plane. This transformation allows us to compute the angular distance between the filament segment and each pixel using only the declination angle. This process is repeated for each segment of a filament, and for all filaments.

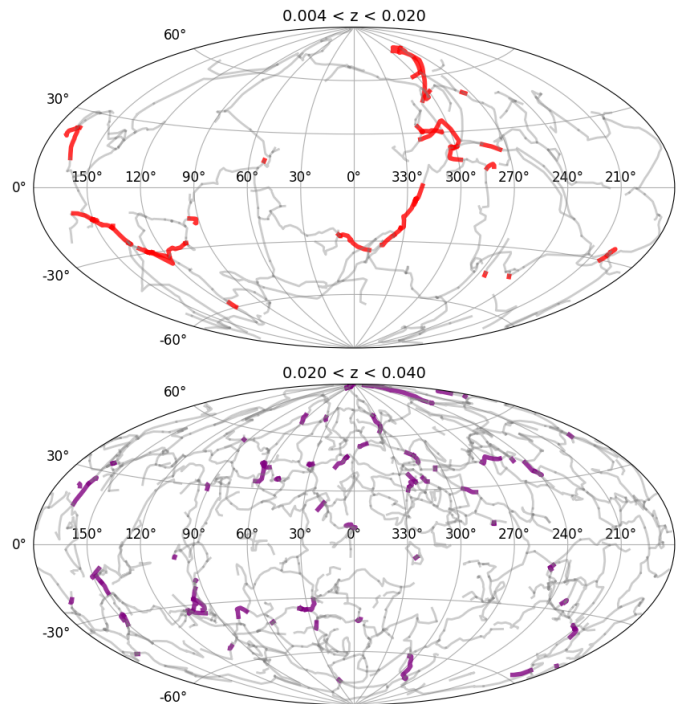


FIG. 1: Projection of 3D filamentary structure on the plane of the sky in the redshift range  $0.004 < z < 0.020$  (upper panel) and  $0.020 < z < 0.040$  (lower panel).

Grey lines correspond to the sky-projection of all filaments, red lines to the densest hexile and purple to the densest decile in their corresponding redshift interval.

## B. Multipole removal

In H2025, we showed that by removing the largest angular scales of the CMB in simulations, the  $S/N$  level of the measured mean temperature around galaxies increased significantly. The reason for this is that the angular scale of the galactic filaments is smaller than the largest CMB fluctuations. The CMB fluctuations at large scale act as noise to the smaller scale fluctuations associated to the galaxies. For the filaments at  $z < 0.02$ , we found in H2025 that by removing the 5 first multipole moments of the CMB maps, we could optimize  $S/N$ . Here we will also consider filaments in the redshift range  $0.02 < z < 0.04$ . A typical massive filament has a total length of about 15 – 20Mpc which corresponds to an angular extension of about 6 – 9 degrees in the sky at these redshifts, but as most of these are curved (as we can see in Fig. 1), their actual angular extension is typically about 5 degrees corresponding to multipoles  $\ell \gtrsim 32$ . We therefore choose to remove all multipoles  $\ell \leq 32$  in both Planck data and simulations for analysis in the redshift range  $0.02 < z < 0.04$ . For the larger filaments in  $z < 0.02$  we will remove  $\ell \leq 5$  as in H2025. To test consistency, we will also apply the analysis to maps with  $\ell > 5$ ,  $\ell > 10$ ,  $\ell > 16$ ,  $\ell > 32$ ,  $\ell > 64$  and  $\ell > 128$ .

The method for estimating the lowest multipole moments outside the mask, and then subtracting is explained in detail in H2025. In short, for the lowest multipole removals  $l \leq 16$ , we calculate and invert the full  $a_{\ell m}$  coupling matrix with the given mask and apply this to the cut-sky  $a_{\ell m}$ . This is the same method used for mono and dipole removal in the Healpix package [26]. For removing higher multipoles, we use a simplified procedure where we downgrade and smooth the map to the resolution corresponding to the maximum multipole to remove. In H2025 we found that the two methods give similar results.

## C. Transversal temperature profiles

As mentioned above, each filament consists of a series of segments that connect critical points in the density field. These structures have an intrinsic cylindrical symmetry so that their projection onto the plane of the sky appear as a rectangle. The previously detected temperature decrement reported in L2023 and H2025 is an order of magnitude smaller than the standard deviation of the CMB temperature fluctuations. We therefore need to stack transversal temperature profiles of filaments in order to reach a sufficiently high  $S/N$  level. Essentially, this stacked profile is obtained by averaging the transverse temperature profiles of each individual filament. In order to calculate the transverse temperature profile of a filament, we need to compute the average temperature within different projected rectangular shells around its axis.

The mean temperature  $\langle \Delta T \rangle(d_{\perp})$  at a perpendicular

distance  $d_{\perp}$  from the filamentary spine taken over all the filaments is calculated by

$$\langle \Delta T \rangle(d_{\perp}^b) = \frac{1}{N_{\text{fil}}} \sum_{k=1}^{N_{\text{fil}}} \left( \frac{1}{N_k} \sum_{i \in C_{bk}} \Delta T(k, i) \right). \quad (1)$$

Where, for a given distance bin  $b$ , and for each filament  $k$ , we take the mean temperature of all  $N_k$  pixels  $i$  within the perpendicular distances  $d_{\perp}$  corresponding to this given distance bin  $b$  for the given filament (i.e. all pixels inside  $C_{bk}$ ). Then, we take the average over those mean values across all filaments  $N_{\text{fil}}$ . The reason for firstly taking mean temperature over each filament is to avoid the filaments with many pixels in a given distance bin to dominate the signal. It is important to clarify that, in our method, each pixel appears at most once per filament. However, since two or more filaments may overlap in their projection onto the sky, pixels that are shared will be considered independently for each filament and could contribute to the profile at different perpendicular distances ( $d_{\perp} < 6$  Mpc). To construct temperature profiles we select equi-spaced bins and apply this method to each of these bins. We have used a bootstrap resampling technique method to assess the intrinsic uncertainty of the temperature profiles obtained. This was accomplished by applying 500 iterations of random resampling to the temperature profiles calculated, in order to obtain the standard deviation of the derived profiles.

## IV. RESULTS

In this section we first present the results in the redshift range  $0.004 < z < 0.020$  which was also used in L2023 and H2025. Then, we extend our analysis to the range  $0.020 < z < 0.040$  testing whether the cooling effect seen in the first redshift range may be visible also at these higher redshifts. Finally, we also consider the total redshift interval  $0.004 < z < 0.040$ . As detailed above, we will present our main results based on maps with  $\ell > 5$  for the range  $0.004 < z < 0.020$ , and  $\ell > 32$  in the more distant ranges  $0.020 < z < 0.040$ . For the full range  $0.004 < z < 0.040$  results of the variance weighted combination of the results of the individual ranges will be presented along with a combined analysis of all filaments in the full range applied to the same CMB map with different multipole cuts.

### A. Subsample percentiles according to linear luminosity density

Firstly, we divide the filaments in tertiles of linear luminosity density and estimate temperature profiles for the densest as well as the least dense tertile. This is shown in the upper panel of Figure 2.

We can see that the values of the temperature in pixels associated to the least dense tertile of filaments



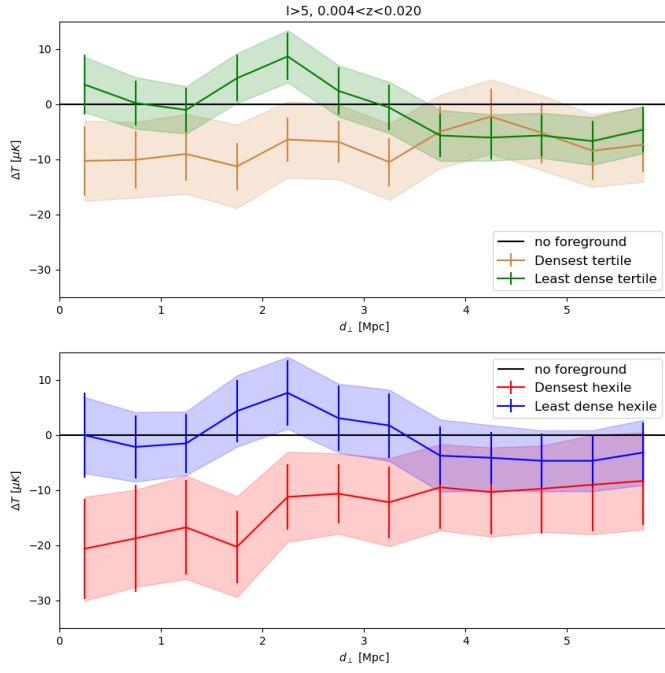


FIG. 2: Mean temperature profiles in perpendicular distances to the filament spine for the redshift range  $0.004 < z < 0.020$ , with  $\ell > 5$ . The solid line is the data, vertical solid lines are the standard deviation of the data and the shadowed regions are the variance in synthetic simulations. In the upper panel the analysis is done for the filaments in the densest and least dense tertile of luminosity density. In the lower panel the analysis is done for the filaments in the densest and least dense hexile of luminosity density.

are consistent with the average CMB values. On the other hand, those associated to the densest tertile show a temperature decrement, presenting a systematic trend with the perpendicular distance to the filament spine. One could argue that this effect is mainly associated to the galaxies on the spine of the filament (as shown in L2023 and H2025). With the aim of addressing the effect of individual galaxies versus the filamentary intergalactic region, we have removed the pixels within 150 projected Kpc from all galaxies in the 2MRS catalog in the redshift range of interest. No significant difference in the transversal temperature profiles was seen. We therefore conclude that the foreground effect is not restricted only to galaxies, but is also associated to the large-scale structures traced by the filaments.

In the lower panel we show the results for filaments belonging to the highest and lowest luminosity density hexile. We can see again a temperature decrement signal for the densest hexile (red line in lower panel) with higher significance respect to the densest tertile (light brown in upper panel). As expected, the significance increases with increasing luminosity density, but we

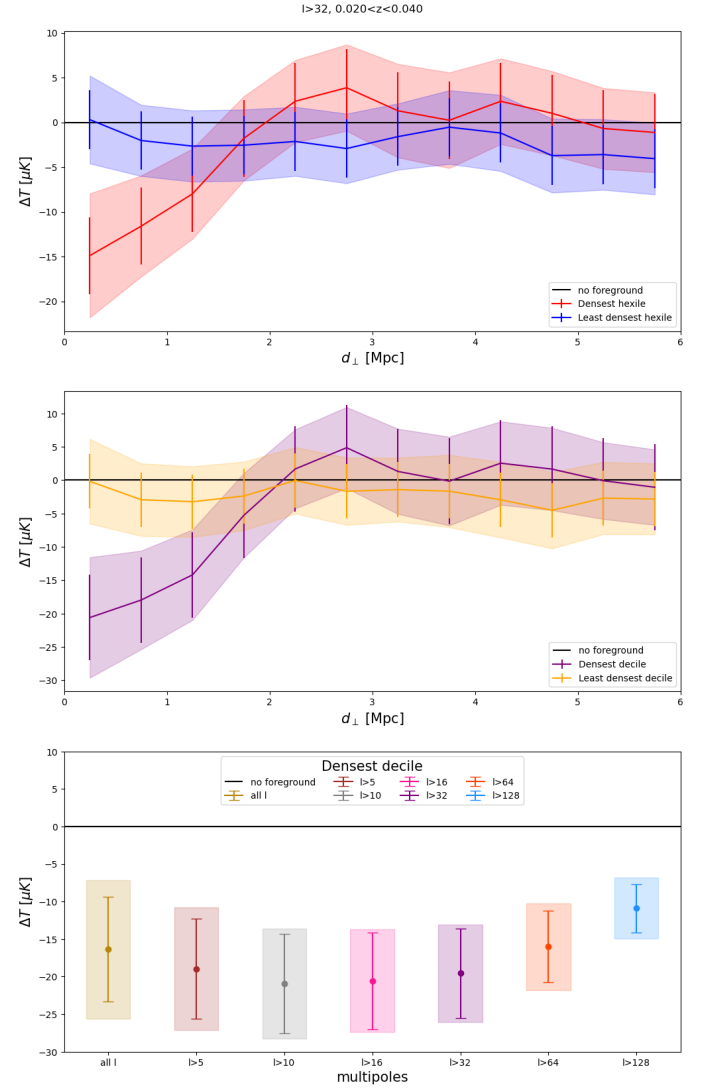


FIG. 3: Analysis of filaments in the redshift range  $0.020 < z < 0.040$ . Upper panel: densest and least dense (luminosity per unit length) hexile filaments. Middle panel: densest and least dense decile filaments. In both panels, the solid line is the data, vertical solid lines are the standard deviation of the data and the shadowed regions are the variance in CMB synthetic simulations. Lower panel: mean temperature of a bin ( $0 - 1.0 \text{ Mpc}$ ) of densest filaments decile, for different ranges of low multipoles removed. The solid vertical lines correspond to the standard deviation of the data, while the shadowed boxes correspond to the variance from CMB synthetic simulations with the same ranges of multipoles removed.

are still far from the significances in H2025. In H2025, the dependency of galaxy morphology and in particular on galaxy mass was taken into account as the CMB temperature was only measured in the late type spiral galaxies with a mass larger than the median mass. In our present approach, although we focus on the more

massive filaments, we use all parts of the filaments, independent of the local variations of mass density along the filament. We argue that the less massive parts of the filaments dilute the signal and give rise to a less significant detection when using the filament centered profile instead of the galaxy centered profile. Also, in H2025, by focusing on massive galaxies and thereby including very dense regions of less massive filaments as well as large overdensities outside the filaments, we also obtained more statistics. The filament based approach is however better for larger distances which is our main focus here, as properties of individual galaxies are less certain at higher redshifts.

As a next step, we have considered a significantly larger volume corresponding to the redshift range  $0.020 < z < 0.040$ . In this redshift range, there is a total of 908 filaments compared to the previous redshift range where a total number of 278 filaments were found. This larger sample of filaments allows for a larger number of sub-samples corresponding to different percentiles. The results are shown in the upper (middle) panels of Figure 3 for the densest and least densest hexile (decile). We can see for this extended redshift range that the signal is restricted to the first bins in transversal distances. We argue that this behavior is related to the smaller angular scale subtended by the filament width at these higher redshifts. As in the previous range, we have also tested the removal of pixels within 150 projected Kpc from the 2MRS galaxies and again there were only tiny differences in the profiles.

The lower panel in this figure shows the mean temperature within 1Mpc as a function of minimum  $\ell$  of the CMB map. We can see that for larger multipole removal, the variance in the synthetic simulation are similar to the data bootstrap-derived standard deviation. For lower values of minimum  $\ell$ , the signal and variance is affected by large angular scales CMB temperature fluctuation. For larger multipole cuts, the CMB temperature in the filaments is gradually getting less negative, but as the variance of the CMB fluctuations are decreasing with increasing multipole cut, the relative temperature difference with respect to the CMB and therefore also the significance of the signal, is almost unchanged.

In the upper part of table I the significances for the densest decile in this redshift interval, up to 2 Mpc, for different multipole removals is shown. We see that for the first distance bin within  $< 0.5$ Mpc, we reach  $\sim 3\sigma$  significance. At a distance of  $< 1.5$ Mpc there is still a significant  $2.5\sigma$  signal, whereas the signal disappears quite abruptly after this as was also seen in the figures. While the maximum significance is found as expected for this redshift range at  $\ell > 32$ , the signal is very consistent also for other multipole cuts.

Finally, we explore the mean temperature taken over

Dist. [Mpc]	Significance ( $\sigma$ ), all angles						
	all $\ell$	$\ell > 5$	$\ell > 10$	$\ell > 16$	$\ell > 32$	$\ell > 64$	$\ell > 128$
0.0 - 0.5	1.79	2.30	2.77	2.88	2.90	2.64	2.49
0.5 - 1.0	1.63	2.22	2.81	2.95	2.96	2.68	2.46
1.0 - 1.5	1.24	1.92	2.50	2.57	2.64	2.22	1.58
1.5 - 2.0	0.20	0.70	1.12	1.04	1.09	0.45	1.03
	Significance ( $\sigma$ ), radially oriented						
	all $\ell$	$\ell > 5$	$\ell > 10$	$\ell > 16$	$\ell > 32$	$\ell > 64$	$\ell > 128$
0.0 - 0.5	2.33	2.56	3.12	3.19	3.22	2.98	2.89
0.5 - 1.0	2.26	2.55	3.30	3.39	3.47	3.26	3.01
1.0 - 1.5	1.59	1.90	2.58	2.67	2.80	2.44	1.46
1.5 - 2.0	0.41	0.62	1.13	1.15	1.20	0.71	0.97

TABLE I: Significances for the filaments of the densest decile of luminosity density in the redshift range  $0.020 < z < 0.040$  per 0.5 Mpc bin. We consider the cases: all  $\ell$ ,  $\ell > 5$ ,  $\ell > 10$ ,  $\ell > 16$ ,  $\ell > 32$ ,  $\ell > 64$  and  $\ell > 128$ . Upper part of table: including all filaments in the decile (as in figure 3, middle panel). Lower part: including only radially oriented filaments (as in figure 6, lower panel)

all filaments in the complete redshift range  $0.004 < z < 0.04$ . In Figure 4 we show the temperature profile for the variance weighted average between the results for the optimal case in each redshift range, the densest hexile for  $0.004 < z < 0.02$  using the multipole cut  $\ell > 5$  and the densest decile for  $0.02 < z < 0.04$  removing  $\ell \leq 32$ . We find a  $\sim 3.5\sigma$  detection for the full range.

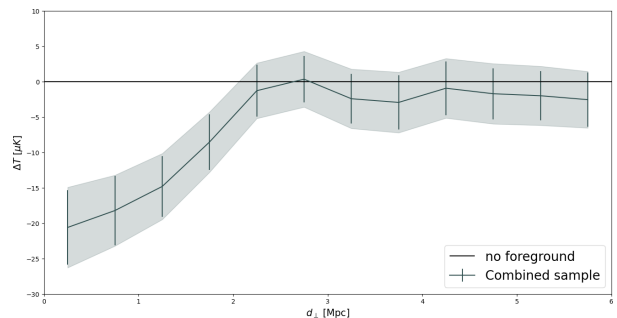


FIG. 4: Temperature profile for the full redshift range  $0.004 < z < 0.04$  as variance weighted combination of the individual ranges based on the densest hexile with  $\ell > 5$  for the lowest redshift range and densest decile with  $\ell > 32$  for the highest redshift range. The solid line is the data, the vertical solid line is the standard deviation of this data and the shadowed regions are the variance in simulations.

## B. Orientation of filaments with respect to the line of sight

In the previous analysis, we have shown that the densest filaments have the strongest effect on the CMB photons. Thus, we expect that those filaments oriented along the direction of the line of sight will also exhibit

a stronger effect since, in this case, photons travel larger distances in filament environments, which could cause a deeper temperature profile in contrast to those preferentially on the plane of the sky.

Here we consider the densest sub-samples of all the previous redshift ranges and analyze these filaments taking into account the angle between the filament and the line of sight. We divide the sample into radial and plane-of-the-sky filaments. We acknowledge the fact that the tracer galaxies from which the filaments are identified are subject to redshift-space distortions. Therefore, the angle  $\phi$  does not exactly reflect the true angle between the filament and the line of sight direction. However, we argue that it is nevertheless a suitable parameter for a simple division of the sample of filaments into these categories. We find that the decrement signal detected is not extremely sensitive to a particular threshold angle dividing into radial and non radial filaments. We show the results for a standard division with threshold  $\phi = 60^\circ$  ( $\cos(\phi) = 0.5$ ).

In figure 5, we show results for the closest redshift interval ( $0.004 < z < 0.020$ ) and  $\ell > 5$  and figure 6 for the more distant redshift range ( $0.020 < z < 0.040$ ) and  $\ell > 32$ . Lastly, figure 7 correspond to the result for the complete redshift interval ( $0.004 < \ell < 0.040$ ). It is remarkable how the radially oriented filaments in all cases (main panels) show a strong (up to  $4\sigma$ ) signal, while there is a corresponding lack of signal for those filaments in the plane of the sky (inset panels). We argue that this is a clear indication that the extragalactic foreground is associated to 3-D large-scale structures along the radial direction, consistent with the arguments given at the beginning of this section.

Finally, to asses the robustness of the results, in the lower part of Table I as well as in Table II we show the significance for the densest decile of the decrement signals within 2 Mpc from the filaments for radially oriented filaments. The first table show results for the distant redshift range, while the latter shows the full  $0.004 < z < 0.040$  range, for various multipole cuts. Note that for the full range, we did not analyze the temperature profiles for all filaments in the full range on the same map, but rather combine results from the individual redshift ranges. The last column shows the corresponding result for the variance weighted combination. We see that the radially oriented filaments show  $3 - 4\sigma$  significances in the first bin. Not unexepctedly, the variance weighted combination of the redshift ranges shows the highest significance at  $4.1\sigma$ , as in this case the multipole range optimizing  $S/N$  for the angular size of filaments in each redshift range is taken into account.

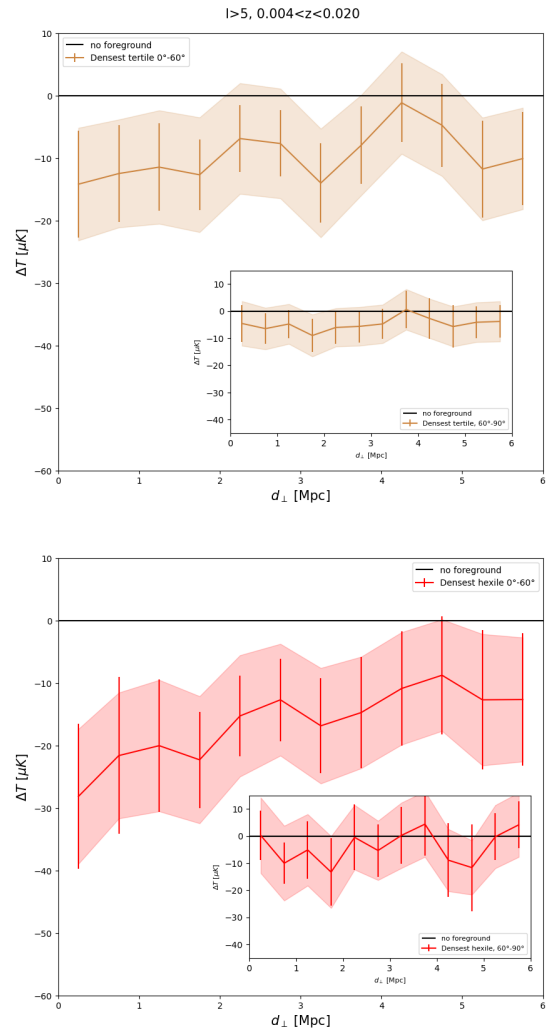


FIG. 5: Filaments in the redshift range  $0.004 < z < 0.020$ , with  $\ell > 5$  for the densest tertile (upper panel) and densest hexile (lower panel) for the preferentially radially oriented filaments ( $\phi < 60^\circ$ ). The inset plot corresponds to the filaments oriented preferentially on the plane of the sky ( $\phi > 60^\circ$ ). The solid line is the data, the vertical solid line is the standard deviation of this data and the shadowed regions are the variance in simulations.

## V. DISCUSSION

Cosmic filaments are common anisotropic structures in the universe, which have been largely studied in both observations and cosmological simulations. The recently detected extragalactic CMB foreground is an unexplained CMB temperature decrement effect associated with galaxies extending to several times the galaxy halo scales (H2023). The geometrically large extension and narrow width of the filaments provide a natural cylindrical coordinate system along the filament spine for studying the possible dependence of the foreground

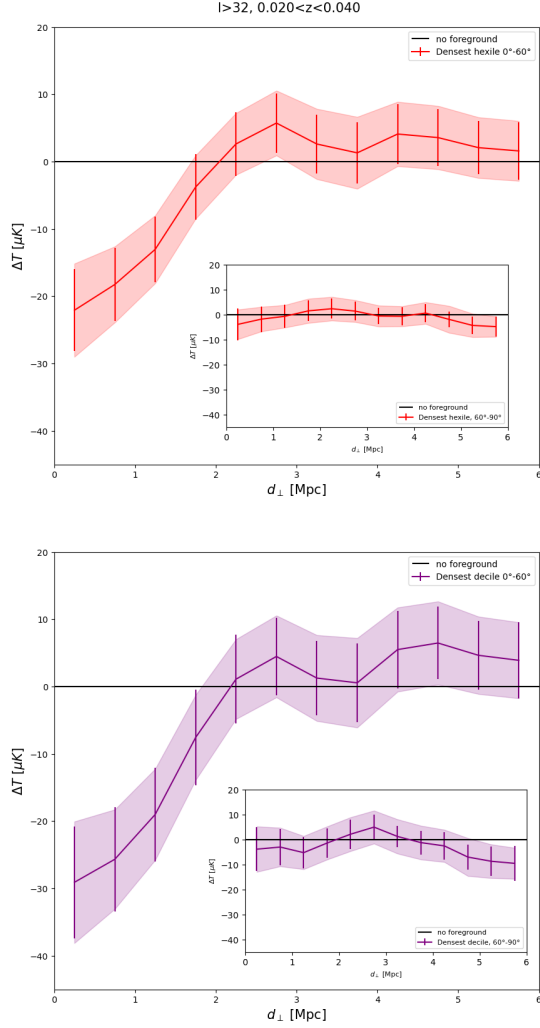


FIG. 6: Filaments in the redshift range  $0.020 < z < 0.040$ , with  $\ell > 32$  for the densest hexile (upper panel) and densest decile (lower panel) for the preferentially radially oriented filaments ( $\phi < 60^\circ$ ). The inset plot corresponds to the filaments oriented preferentially on the plane of the sky ( $\phi > 60^\circ$ ). The solid line is the data, the vertical solid line is the standard deviation of this data and the shadowed regions are the variance in simulations.

effect from filaments. We have therefore analyzed the mean CMB temperature decrement of the SMICA map pixel temperatures as a function of the cylindrical radial coordinate perpendicular to the filament spine in samples obtained in the nearby universe as traced by the 2MRS galaxies.

In this paper, by using temperature profiles around nearby galactic filaments instead of the galaxies themselves, we have discovered several new properties of this unknown CMB cooling mechanism and confirmed its existence independently through the analysis of new and independent galaxy samples. We can summarize these

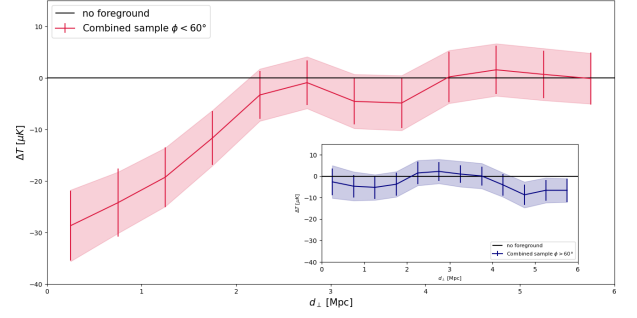


FIG. 7: Temperature profile for the full redshift range  $0.004 < z < 0.04$  for the preferentially radially oriented filaments ( $\phi < 60^\circ$ ). The results for the full range is obtained as a variance weighted combination of the individual ranges based on the densest hexile with  $\ell > 5$  for the lowest redshift range and densest decile with  $\ell > 32$  for the highest redshift range. The inset plot corresponds to the filaments oriented preferentially on the plane of the sky ( $\phi > 60^\circ$ ). The solid line is the data, the vertical solid line is the standard deviation of this data and the shadowed regions are the variance in simulations.

Dist. [Mpc]	Significance ( $\sigma$ )							
	all $\ell$	$\ell > 5$	$\ell > 10$	$\ell > 16$	$\ell > 32$	$\ell > 64$	$\ell > 128$	comb
0.0 - 0.5	2.74	3.18	3.34	3.38	3.51	3.29	3.45	4.14
0.5 - 1.0	2.65	3.20	3.52	3.56	3.75	3.63	3.46	4.07
1.0 - 1.5	2.19	2.72	3.04	3.10	3.25	2.98	2.18	3.39
1.5 - 2.0	1.46	1.77	1.97	2.10	2.15	1.55	0.1	2.17

TABLE II: Significances for the filaments of the densest decile, radially oriented, in the total redshift range  $0.004 < z < 0.040$  (figure 7) per 0.5 Mpc bin. We consider the cases: all  $\ell$ ,  $\ell > 5$ ,  $\ell > 10$ ,  $\ell > 16$ ,  $\ell > 32$ ,  $\ell > 64$  and  $\ell > 128$ . The last column corresponds to the variance weighted combination of the individual ranges based on the densest hexile with  $\ell > 5$  for the lowest redshift range and densest decile with  $\ell > 32$  for the highest redshift range.

new findings in four main points:

- Previous papers have detected the CMB temperature decrement mainly in and around the galactic halos and attributed extended signals to neighbouring galaxies (but see [16] where the signal is correlated to the dark matter density). Here we show that there seem to be a CMB decrement signal associated to the filamentary structure itself and thereby possibly to the density field. By masking a radius of 150Kpc around the galaxies, the filamentary temperature decrement profiles are almost unchanged.
- Previous detections of the cooling of CMB photons in galaxies have been limited to the very nearest universe  $z < 0.02$ . Here we analyze the next red-



shift shell  $0.02 < z < 0.04$  and find, using the temperature profile around filaments, an even stronger signal than in  $z < 0.02$ . The effect is now confirmed independently in a new redshift range at the  $3 - 4\sigma$  level.

- While some dependence of the effect on galactic mass has been discussed in previous works, here we show a very strong dependence on the filamentary mass. We have considered a measure of the K-band luminosity density per unit length within 4 Mpc from the filament spine as a proxy to the filament mass density per unit length. Such measure provides a parameter to distinguish between the densest filaments which trace the large scale structure, and the less dense which more generally reside in void environments. Thus, both the mass content of these two filament types and their dynamical stage are expected to differ significantly. We find a clear trend of larger temperature decrements the higher the filamentary mass and conversely, no signal in the less dense filaments.
- We have taken into account the 3-D shape of filaments and have explored the fact that it would be expected that the filaments produce a larger signal when they are oriented along the line of sight with respect to those on the plane of the sky. The results of these tests regarding the orientation of filaments are also conclusive, most of the signal comes from filaments preferentially oriented along the line of sight, giving an additional strong argument for the

association of the foreground detection to filaments.

As shown in H2025, there is no frequency dependence of the new extragalactic foreground. We confirm this here for the redshift range  $0.02 < z < 0.04$ , finding a  $1 - 2\mu\text{K}$  difference for the mean temperature  $0 - 1$  Mpc from the filament spine between SEVEM 100GHz and 217GHz maps. This difference is consistent with the expected tSZ effect for these filaments. Therefore, an explanation in terms of an interaction with baryons is hard to reconcile with the observations. An alternative explanations for the temperature decrement effect could rely either on CMB photon-dark matter interactions along filaments, or on an anomalous ISW effect associated to the filament gravitational potential evolution as we notice in H2025b.

## ACKNOWLEDGMENTS

Results in this letter are based on observations obtained with Planck (<http://www.esa.int/Planck>), an ESA science mission with instruments and contributions directly funded by ESA Member States, NASA, and Canada. We acknowledge the use of NASA’s WMAP data from the Legacy Archive for Microwave Background Data Analysis (LAMBDA), part of the High Energy Astrophysics Science Archive Center (HEASARC). The simulations were performed on resources provided by UNINETT Sigma2 - the National Infrastructure for High Performance Computing and Data Storage in Norway”. Some of the results in this letter have been derived using the HEALPix package [26]

- 
- [1] G. F. Smoot, C. L. Bennett, A. Kogut, E. L. Wright, J. Aymon, N. W. Boggess, E. S. Cheng, G. de Amici, S. Gulkis, M. G. Hauser, G. Hinshaw, P. D. Jackson, M. Janssen, E. Kaita, T. Kelsall, P. Keegstra, C. Lineweaver, K. Loewenstein, P. Lubin, J. Mather, S. S. Meyer, S. H. Moseley, T. Murdock, L. Rokke, R. F. Silverberg, L. Tenorio, R. Weiss, and D. T. Wilkinson, Structure in the COBE Differential Microwave Radiometer First-Year Maps, *Astrophys. J. Let.* **396**, L1 (1992).
  - [2] P. J. E. Peebles, *The large-scale structure of the universe* (1980).
  - [3] J. R. Bond, L. Kofman, and D. Pogosyan, How filaments of galaxies are woven into the cosmic web, *Nature (London)* **380**, 603 (1996), [arXiv:astro-ph/9512141](https://arxiv.org/abs/astro-ph/9512141) [astro-ph].
  - [4] M. Cautun, R. van de Weygaert, B. J. T. Jones, and C. S. Frenk, Evolution of the cosmic web, *Mon. Not. R. Astron. Soc.* **441**, 2923 (2014), [arXiv:1401.7866](https://arxiv.org/abs/1401.7866) [astro-ph.CO].
  - [5] D. Galárraga-Espinosa, C. Cadiou, C. Gouin, S. D. M. White, V. Springel, R. Pakmor, B. Hadzhiyska, S. Bose, F. Ferlito, L. Hernquist, R. Kannan, M. Barrera, A. Maria Delgado, and C. Hernández-Aguayo, Evolution of cosmic filaments in the MTNG simulation, *Astron. Astroph.* **684**, A63 (2024), [arXiv:2309.08659](https://arxiv.org/abs/2309.08659) [astro-ph.CO].
  - [6] W. Wang, P. Wang, H. Guo, X. Kang, N. I. Libeskind, D. Galárraga-Espinosa, V. Springel, R. Kannan, L. Hernquist, R. Pakmor, H.-R. Yu, S. Bose, Q. Guo, L. Yu, and C. Hernández-Aguayo, The boundary of cosmic filaments, *Mon. Not. R. Astron. Soc.* **532**, 4604 (2024), [arXiv:2402.11678](https://arxiv.org/abs/2402.11678) [astro-ph.CO].
  - [7] K. Kraljic, S. Arnouts, C. Pichon, C. Laigle, S. de la Torre, D. Vibert, C. Cadiou, Y. Dubois, M. Treyer, C. Schmid, S. Codis, V. de Lapparent, J. Devriendt, H. S. Hwang, D. Le Borgne, N. Malavasi, B. Milliard, M. Musso, D. Pogosyan, M. Alpaslan, J. Bland-Hawthorn, and A. H. Wright, Galaxy evolution in the metric of the cosmic web, *Mon. Not. R. Astron. Soc.* **474**, 547 (2018), [arXiv:1710.02676](https://arxiv.org/abs/1710.02676) [astro-ph.GA].
  - [8] C. Laigle, C. Pichon, S. Arnouts, H. J. McCracken, Y. Dubois, J. Devriendt, A. Slyz, D. Le Borgne, A. Benoit-Lévy, H. S. Hwang, O. Ilbert, K. Kraljic, N. Malavasi, C. Park, and D. Vibert, COSMOS2015 photometric redshifts probe the impact of filaments on galaxy properties, *Mon. Not. R. Astron. Soc.* **474**, 5437 (2018), [arXiv:1702.08810](https://arxiv.org/abs/1702.08810) [astro-ph.GA].
  - [9] D. Galárraga-Espinosa, M. Langer, and N. Aghanim, Relative distribution of dark matter, gas, and stars around cosmic filaments in the illustrisng simulation, *Astronomy & Astrophysics* **661**, A115 (2022).

- [10] H. Tanimura, N. Aghanim, V. Bonjean, N. Malavasi, and M. Douspis, Density and temperature of cosmic-web filaments on scales of tens of megaparsecs, *Astron. Astroph.* **637**, A41 (2020), [arXiv:1911.09706 \[astro-ph.CO\]](#).
- [11] J. Kollmeier, S. F. Anderson, G. A. Blanc, M. R. Blanton, K. R. Covey, J. Crane, N. Drory, P. M. Frinchaboy, C. S. Froning, J. A. Johnson, J. P. Kneib, K. Kreckel, A. Merloni, E. W. Pellegrini, R. W. Pogge, S. V. Ramirez, H. W. Rix, C. Sayres, J. Sánchez-Gallego, Y. Shen, A. Tkachenko, J. R. Trump, S. E. Tuttle, A. Weijmans, G. Zasowski, B. Barbuy, R. L. Beaton, M. Bergemann, J. J. Bochanski, W. N. Brandt, A. R. Casey, B. A. Cherinka, M. Eracleous, X. Fan, R. A. García, P. J. Green, S. Hekker, R. R. Lane, P. Longa-Peña, S. Mathur, A. Meza, I. Minchev, A. D. Myers, D. L. Nidever, C. Nitschelm, J. E. O’Connell, A. M. Price-Whelan, M. J. Raddick, G. Rossi, R. Sankrit, J. D. Simon, A. M. Stutz, Y. S. Ting, B. Trakhtenbrot, B. A. Weaver, C. N. A. Willmer, and D. H. Weinberg, SDSS-V Pioneering Panoptic Spectroscopy, in *Bulletin of the American Astronomical Society*, Vol. 51 (2019) p. 274.
- [12] H. E. Luparello, E. F. Boero, M. Lares, A. G. Sánchez, and D. G. Lambas, The cosmic shallows – i. interaction of cmb photons in extended galaxy haloes, *Monthly Notices of the Royal Astronomical Society* **518**, 5643–5652 (2022).
- [13] F. K. Hansen, E. F. Boero, H. E. Luparello, and D. Garcia Lambas, A possible common explanation for several cosmic microwave background (cmb) anomalies: A strong impact of nearby galaxies on observed large-scale cmb fluctuations, *Astronomy & Astrophysics* **675**, L7 (2023).
- [14] F. K. Hansen, D. Garcia Lambas, H. E. Luparello, F. Toscano, and L. A. Pereyra, A  $p < 0.0001$  detection of cosmic microwave background cooling in galactic halos and its possible relation to dark matter, *Astron. Astroph.* **696**, A184 (2025), [arXiv:2411.15307 \[astro-ph.CO\]](#).
- [15] D. G. Lambas, F. K. Hansen, F. Toscano, H. E. Luparello, and E. F. Boero, The CMB Cold Spot as predicted by foregrounds around nearby galaxies, *aap* **681**, A2 (2024), [arXiv:2310.13755 \[astro-ph.CO\]](#).
- [16] M. Cruz, E. Martínez-González, C. Gimeno-Amo, B. J. Kavanagh, and M. Tucci, Unexplained correlation between the Cosmic Microwave Background temperature and the local matter density distribution, *jcap* **2025**, 079 (2025), [arXiv:2407.17599 \[astro-ph.CO\]](#).
- [17] F. Toscano, F. K. Hansen, D. Garcia Lambas, H. Luparello, P. Fosalba, and E. Gaztañaga, Are CMB derived cosmological parameters affected by foregrounds associated to nearby galaxies?, *Physical Review D* **111**, 083528 (2025), [arXiv:2410.24026 \[astro-ph.CO\]](#).
- [18] <http://tdc-www.harvard.edu/2mrs/>.
- [19] J. P. Huchra, L. M. Macri, K. L. Masters, T. H. Jarrett, P. Berlind, M. Calkins, A. C. Crook, R. Cutri, P. Erdogdu, E. Falco, T. George, C. M. Hutcheson, O. Lahav, J. Mader, J. D. Mink, N. Martimbeau, S. Schneider, M. Skrutskie, S. Tokarz, and M. Westover, the 2Mass Redshift Survey -Description and Data Release, *ApJS* **199**, 26 (2012), [arXiv:arXiv:1108.0669v1](#).
- [20] T. Sousbie, The persistent cosmic web and its filamentary structure - I. Theory and implementation, *Mon. Not. R. Astron. Soc.* **414**, 350 (2011), [arXiv:1009.4015](#).
- [21] T. Sousbie, C. Pichon, and H. Kawahara, The persistent cosmic web and its filamentary structure - II. Illustrations, *Mon. Not. R. Astron. Soc.* **414**, 384 (2011), [arXiv:1009.4014](#).
- [22] Planck Collaboration, N. Aghanim, Y. Akrami, M. Ashdown, J. Aumont, C. Baccigalupi, M. Ballardini, A. J. Banday, R. B. Barreiro, N. Bartolo, S. Basak, R. Battye, K. Benabed, J. P. Bernard, M. Bersanelli, P. Bielewicz, J. J. Bock, J. R. Bond, J. Borrill, F. R. Bouchet, F. Boulanger, M. Bucher, C. Burigana, R. C. Butler, E. Calabrese, J. F. Cardoso, J. Carron, A. Challinor, H. C. Chiang, J. Chluba, L. P. L. Colombo, C. Combet, D. Contreras, B. P. Crill, F. Cuttaia, P. de Bernardis, G. de Zotti, J. Delabrouille, J. M. Delouis, E. Di Valentino, J. M. Diego, O. Doré, M. Douspis, A. Ducout, X. Dupac, S. Dusini, G. Efstathiou, F. Elsner, T. A. Enßlin, H. K. Eriksen, Y. Fantaye, M. Farhang, J. Fergusson, R. Fernandez-Cobos, F. Finelli, F. Forastieri, M. Frailis, A. A. Fraisse, E. Franceschi, A. Frolov, S. Galeotta, S. Galli, K. Ganga, R. T. Génova-Santos, M. Gerbino, T. Ghosh, J. González-Nuevo, K. M. Górski, S. Gratton, A. Gruppuso, J. E. Gudmundsson, J. Hamann, W. Handley, F. K. Hansen, D. Herranz, S. R. Hildebrandt, E. Hivon, Z. Huang, A. H. Jaffe, W. C. Jones, A. Karakci, E. Keihänen, R. Kesitalo, K. Kiiveri, J. Kim, T. S. Kisner, L. Knox, N. Krachmalnicoff, M. Kunz, H. Kurki-Suonio, G. Lagache, J. M. Lamarre, A. Lasenby, M. Lattanzi, C. R. Lawrence, M. Le Jeune, P. Lemos, J. Lesgourgues, F. Levrier, A. Lewis, M. Liguori, P. B. Lilje, M. Lilley, V. Lindholm, M. López-Caniego, P. M. Lubin, Y. Z. Ma, J. F. Macías-Pérez, G. Maggio, D. Maino, N. Mandolesi, A. Mangilli, A. Marcos-Caballero, M. Maris, P. G. Martin, M. Martinelli, E. Martínez-González, S. Matarrese, N. Mauri, J. D. McEwen, P. R. Meinhold, A. Melchiorri, A. Mennella, M. Migliaccio, M. Millea, S. Mitra, M. A. Miville-Deschênes, D. Molinari, L. Montier, G. Morgante, A. Moss, P. Natoli, H. U. Nørgaard-Nielsen, L. Pagano, D. Paoletti, B. Partridge, G. Patanchon, H. V. Peiris, F. Perrotta, V. Pettorino, F. Piacentini, L. Polastri, G. Polenta, J. L. Puget, J. P. Rachen, M. Reinecke, M. Remazeilles, A. Renzi, G. Rocha, C. Rosset, G. Roudier, J. A. Rubiño-Martín, B. Ruiz-Granados, L. Salvati, M. Sandri, M. Savelainen, D. Scott, E. P. S. Shellard, C. Sirignano, G. Sirri, L. D. Spencer, R. Sunyaev, A. S. Suur-Uski, J. A. Tauber, D. Tavagnacco, M. Tenti, L. Toffolatti, M. Tomasi, T. Trombetti, L. Valenziano, J. Valiviita, B. Van Tent, L. Vibert, P. Vielva, F. Villa, N. Vittorio, B. D. Wandelt, I. K. Wehus, M. White, S. D. M. White, A. Zacchei, and A. Zonca, Planck 2018 results. VI. Cosmological parameters, *Astron. Astroph.* **641**, A6 (2020), [arXiv:1807.06209 \[astro-ph.CO\]](#).
- [23] Planck Collaboration, N. Aghanim, Y. Akrami, F. Arroja, M. Ashdown, J. Aumont, C. Baccigalupi, M. Ballardini, A. J. Banday, R. B. Barreiro, N. Bartolo, S. Basak, R. Battye, K. Benabed, J. P. Bernard, M. Bersanelli, P. Bielewicz, J. J. Bock, J. R. Bond, J. Borrill, F. R. Bouchet, F. Boulanger, M. Bucher, C. Burigana, R. C. Butler, E. Calabrese, J. F. Cardoso, J. Carron, B. Casaponsa, A. Challinor, H. C. Chiang, L. P. L. Colombo, C. Combet, D. Contreras, B. P. Crill, F. Cuttaia, P. de Bernardis, G. de Zotti, J. Delabrouille, J. M. Delouis, F. X. Désert, E. Di Valentino, C. Dickinson, J. M. Diego, S. Donzelli, O. Doré, M. Douspis, A. Ducout, X. Dupac, G. Efstathiou, F. Elsner, T. A. Enßlin, H. K. Eriksen,

- E. Falgarone, Y. Fantaye, J. Fergusson, R. Fernandez-Cobos, F. Finelli, F. Forastieri, M. Frailis, E. Franceschi, A. Frolov, S. Galeotta, S. Galli, K. Ganga, R. T. Génova-Santos, M. Gerbino, T. Ghosh, J. González-Nuevo, K. M. Górski, S. Gratton, A. Gruppuso, J. E. Gudmundsson, J. Hamann, W. Handley, F. K. Hansen, G. Helou, D. Herranz, S. R. Hildebrandt, E. Hivon, Z. Huang, A. H. Jaffe, W. C. Jones, A. Karakci, E. Keihänen, R. Keskitalo, K. Kiiveri, J. Kim, T. S. Kisner, L. Knox, N. Krachmalnicoff, M. Kunz, H. Kurki-Suonio, G. Lagache, J. M. Lamarre, M. Langer, A. Lasenby, M. Lattanzi, C. R. Lawrence, M. Le Jeune, J. P. Leahy, J. Lesgourgues, F. Levrier, A. Lewis, M. Liguori, P. B. Lilje, M. Lilley, V. Lindholm, M. López-Caniego, P. M. Lubin, Y. Z. Ma, J. F. Macías-Pérez, G. Maggio, D. Maino, N. Mandolesi, A. Mangilli, A. Marcos-Caballero, M. Maris, P. G. Martin, M. Martinelli, E. Martínez-González, S. Matarrese, N. Mauri, J. D. McEwen, P. D. Meerburg, P. R. Meinhold, A. Melchiorri, A. Mennella, M. Migliaccio, M. Millea, S. Mitra, M. A. Miville-Deschênes, D. Molinari, A. Moneti, L. Montier, G. Morgante, A. Moss, S. Mottet, M. Münchmeyer, P. Natoli, H. U. Nørgaard-Nielsen, C. A. Oxborrow, L. Pagano, D. Paoletti, B. Partridge, G. Patanchon, T. J. Pearson, M. Peel, H. V. Peiris, F. Perrotta, V. Pettorino, F. Piacentini, L. Polastri, G. Polenta, J. L. Puget, J. P. Rachen, M. Reinecke, M. Remazeilles, C. Renault, A. Renzi, G. Rocha, C. Rosset, G. Roudier, J. A. Rubiño-Martín, B. Ruiz-Granados, L. Salvati, M. Sandri, M. Savelainen, D. Scott, E. P. S. Shellard, M. Shiraishi, C. Sirignano, G. Sirri, L. D. Spencer, R. Sunyaev, A. S. Suur-Uski, J. A. Tauber, D. Tavagnacco, M. Tenti, L. Terenzi, L. Toffolatti, M. Tomasi, T. Trombetti, J. Valiviita, B. Van Tent, L. Vibert, P. Vielva, F. Villa, N. Vittorio, B. D. Wandelt, I. K. Wehus, M. White, S. D. M. White, A. Zacchei, and A. Zonca, Planck 2018 results. I. Overview and the cosmological legacy of Planck, *Astron. Astroph.* **641**, A1 (2020), [arXiv:1807.06205 \[astro-ph.CO\]](https://arxiv.org/abs/1807.06205).
- [24] <https://pla.esac.esa.int/#maps>.
- [25] Planck Collaboration, Y. Akrami, M. Ashdown, J. Aumont, C. Baccigalupi, M. Ballardini, A. J. Banday, R. B. Barreiro, N. Bartolo, S. Basak, K. Benabed, M. Bersanelli, P. Bielewicz, J. R. Bond, J. Borrill, F. R. Bouchet, F. Boulanger, M. Bucher, C. Burigana, E. Calabrese, J. F. Cardoso, J. Carron, B. Casaponsa, A. Challinor, L. P. L. Colombo, C. Combet, B. P. Crill, F. Cuttaia, P. de Bernardis, A. de Rosa, G. de Zotti, J. Delabrouille, J. M. Delouis, E. Di Valentino, C. Dickinson, J. M. Diego, S. Donzelli, O. Doré, A. Ducout, X. Dupac, G. Efstathiou, F. Elsner, T. A. Enßlin, H. K. Eriksen, E. Falgarone, R. Fernandez-Cobos, F. Finelli, F. Forastieri, M. Frailis, A. A. Fraisse, E. Franceschi, A. Frolov, S. Galeotta, S. Galli, K. Ganga, R. T. Génova-Santos, M. Gerbino, T. Ghosh, J. González-Nuevo, K. M. Górski, S. Gratton, A. Gruppuso, J. E. Gudmundsson, W. Handley, F. K. Hansen, G. Helou, D. Herranz, S. R. Hildebrandt, Z. Huang, A. H. Jaffe, A. Karakci, E. Keihänen, R. Keskitalo, K. Kiiveri, J. Kim, T. S. Kisner, N. Krachmalnicoff, M. Kunz, H. Kurki-Suonio, G. Lagache, J. M. Lamarre, A. Lasenby, M. Lattanzi, C. R. Lawrence, M. Le Jeune, F. Levrier, M. Liguori, P. B. Lilje, V. Lindholm, M. López-Caniego, P. M. Lubin, Y. Z. Ma, J. F. Macías-Pérez, G. Maggio, D. Maino, N. Mandolesi, A. Mangilli, A. Marcos-Caballero, M. Maris, P. G. Martin, E. Martínez-González, S. Matarrese, N. Mauri, J. D. McEwen, P. R. Meinhold, A. Melchiorri, A. Mennella, M. Migliaccio, M. A. Miville-Deschênes, D. Molinari, A. Moneti, L. Montier, G. Morgante, P. Natoli, F. Opizzi, L. Pagano, D. Paoletti, B. Partridge, M. Peel, V. Pettorino, F. Piacentini, G. Polenta, J. L. Puget, J. P. Rachen, M. Reinecke, M. Remazeilles, A. Renzi, G. Rocha, G. Roudier, J. A. Rubiño-Martín, B. Ruiz-Granados, L. Salvati, M. Sandri, M. Savelainen, D. Scott, D. S. Seljebotn, C. Sirignano, L. D. Spencer, A. S. Suur-Uski, J. A. Tauber, D. Tavagnacco, M. Tenti, H. Thommesen, L. Toffolatti, M. Tomasi, T. Trombetti, J. Valiviita, B. Van Tent, P. Vielva, F. Villa, N. Vittorio, B. D. Wandelt, I. K. Wehus, A. Zacchei, and A. Zonca, Planck 2018 results. IV. Diffuse component separation, *Astron. Astroph.* **641**, A4 (2020), [arXiv:1807.06208 \[astro-ph.CO\]](https://arxiv.org/abs/1807.06208).
- [26] K. M. Górski, E. Hivon, A. J. Banday, B. D. Wandelt, F. K. Hansen, M. Reinecke, and M. Bartelmann, HEALPix: A Framework for High-Resolution Discretization and Fast Analysis of Data Distributed on the Sphere, *Astrophys. J.* **622**, 759 (2005), [arXiv:astro-ph/0409513 \[astro-ph\]](https://arxiv.org/abs/astro-ph/0409513).
- [27] <https://healpix.sourceforge.io/>.